

## A Relationship between Reflectivity and Snow Rate for a High-Altitude S-Band Radar

JONATHAN P. WOLFE

*National Weather Service, Portland, Oregon*

JEFFERSON R. SNIDER

*Department of Atmospheric Science, University of Wyoming, Laramie, Wyoming*

(Manuscript received 23 May 2011, in final form 29 December 2011)

### ABSTRACT

An important application of radar reflectivity measurements is their interpretation as precipitation intensity. Empirical relationships exist for converting microwave backscatter retrieved from precipitation particles (represented by an equivalent reflectivity factor  $Z_e$ ) to precipitation intensity. The reflectivity–snow-rate relationship has the form  $Z_e = \alpha S^\beta$ , where  $S$  is a liquid-equivalent snow rate and  $\alpha$  and  $\beta$  are fitted coefficients. Substantial uncertainty exists in radar-derived values of snow rate because the reflectivity and intensity associated with snow tend to be smaller than those for rain and because of snow-particle drift between radar and surface detection. Uncertainty in radar-derived snow rate is especially evident at the few available high-altitude sites for which a relationship between reflectivity and snow rate has been developed. Using a new type of precipitation sensor and a National Weather Service radar, this work investigates the  $Z_e$ – $S$  relationship at a high-altitude site (Cheyenne, Wyoming). The  $S$  measurements were made 25 km northwest of the radar on the eastern flank of the Rocky Mountains; vertical separation between the radar range gate and the ground was less than 700 m. A meteorological feature of the snowstorms was northeasterly upslope flow of humid air at low levels. The  $Z_e$ – $S$  data pairs were fitted with  $\beta = 2$ . The finding of this study for Cheyenne,  $\alpha = 110 \text{ mm}^4 \text{ h}^2 \text{ m}^{-3}$ , is bounded by previous determinations made at other high-altitude National Weather Service sites. Also investigated was the temperature dependence of  $\alpha$ . A positive  $\alpha$ – $T$  relationship is evident and is hypothesized to result from ice crystals produced by heterogeneous ice nucleation, at cloud top, followed by diffusional crystal growth during sedimentation.

### 1. Introduction

In the western United States, snowfall is measured by a network of gauges that includes measurements made at National Weather Service (NWS) offices, at snow-telemetry sites (SNOTEL), and by Community Collaborative Rain, Hail and Snow (CoCoRaHS) observers. Despite the large number of monitoring sites, the network does not adequately resolve the spatial and temporal variability of snowfall needed for many practical and research applications. This is the case for both rainfall and snowfall, but for the latter there are additional complications stemming from the smaller intensity associated with snowfall and the inefficient gauge catch of particles with small air/ice density (e.g., unrimed ice

particles) (Sevruk 1996; Groisman and Legates 1994). The latter problem is enhanced in the Rocky Mountain region, where the air/ice density of the snow is generally small (Judson and Doesken 2000; Wetzel et al. 2004) and where wind drifting of snow is common (Schmidt 1982).

Radar is an alternative to a network of precipitation gauges. Radar retrieval of the equivalent reflectivity factor  $Z_e$ , combined with a  $Z_e$ – $S$  relationship, provides a liquid-equivalent snow rate  $S$  over large domains ( $\sim 10^5 \text{ km}^2$ ) and with high spatial and temporal resolution (Boucher and Wieler 1985; Fujiiyoshi et al. 1990; Rasmussen et al. 2003). A disadvantage of this approach is that terrain limits the retrieval of  $Z_e$  from the lowest levels of wintertime storms, and this terrain effect can lead to significant error in radar-derived snow rates at the ground (Super and Holroyd 1998; Vignal et al. 2000; Brown et al. 2002; Wood et al. 2003). In addition, horizontal drift of falling snow decorrelates the  $Z_e$ – $S$  pairs used to develop a  $Z_e$ – $S$  relationship (Rasmussen et al. 2003). Because of these limitations, a suite of measurement

---

*Corresponding author address:* Jefferson R. Snider, Dept. of Atmospheric Science, University of Wyoming, Dept. 3038, 1000 E Univ. Ave., Laramie, WY 82071.  
E-mail: jsnider@uwyo.edu

systems—including radar and precipitation gauges—is used to estimate snow rate and snow accumulation in the mountainous western United States (Wetzel et al. 2004).

Radar has been used to infer precipitation intensity for over 65 years [for a review, see Joss and Waldvogel (1990)], but, despite its legacy, substantial uncertainty remains in the relationship between reflectivity and intensity—in particular, for snow. Recent progress has been spurred by many innovations: 1) range-dependent correlations that correct from reflectivity aloft to a snow rate at the surface (Super and Holroyd 1998; Vignal et al. 2000); 2) volume-scanning strategies that enable mountaintop radar systems to sample a larger fraction of the lower atmosphere (Brown et al. 2002; Wood et al. 2003); 3) airborne radars that retrieve  $Z_e$  at nearly the same location as in situ measurement of  $S$ , thus eliminating the decorrelation that results from the horizontal drift of falling snow (Pokharel and Vali 2011); 4) ground-based Doppler radar systems that discriminate between aggregate and rimed snow (Moismann 1995; Matrosov et al. 2008), enabling selection of the appropriate  $Z_e$ – $S$  relationship (Rasmussen et al. 2003); and 5) the development of improved surface-based snowfall sensors (Rasmussen et al. 2011).

We report on surface snow-rate measurements coordinated with retrievals of  $Z_e$  from an NWS radar (the radar is described in section 2d). At the surface, we made measurements of snow rate using a device akin to the heated-wire sensor developed for measurement of cloud liquid water content (King et al. 1980; Rasmussen et al. 2011). Hereinafter, we refer to that sensor as the Hotplate.<sup>1</sup> We deployed the Hotplate 25 km northwest of the Cheyenne, Wyoming, NWS radar and used the acquired data to develop an empirical  $Z_e$ – $S$  relationship.

Our work is presented in the following sequence. We begin with descriptions of the measurement systems (section 2) and then present a hypothesized correlation between  $\alpha$  and temperature (section 3). What follows (section 4) is our presentation of the radar reflectivity data and an analysis of the low-level  $Z_e$  vertical gradient. In section 5, we fit the  $Z_e$ – $S$  measurements, present the deduced  $Z_e$ – $S$  relationship, analyze two case studies, and investigate the hypothesized  $\alpha$ – $T$  correlation. In the final part of section 5, we compare the radar-derived 24-h accumulations with an independent set of gauge accumulations (from CoCoRaHS and NWS). Our conclusions are summarized in section 6, and in the appendix we explain the statistical methods used to deduce the  $Z_e$ – $S$  relationship.

<sup>1</sup> Hotplate is a registered trademark of the University Corporation for Atmospheric Research (UCAR) Foundation. See section 2 for a description of the instrument.

## 2. Measurements

Five snowstorms were monitored during February and March of 2006. At the surface, these storms were characterized by an anticyclone positioned over south-central Canada that caused northeasterly upslope winds to occur at Cheyenne. Precipitation from these systems is enhanced by flow outward from the center of the anticyclone, pushing humid low-level air westward over the eastern flank of the Rocky Mountains (Boatman and Reinking 1984).

Reflectivity maps from the Cheyenne radar were analyzed for bright banding, which would indicate a snow-particle melting layer aloft (Rogers and Yau 1989). Bright banding was not detected, and so we concluded that snow-particle melting was not significant for the five Cheyenne snowstorms.

We present data from eight study days. These are 15 and 16 February (snowstorm 1), 8 March (snowstorm 2), 10 and 11 March (snowstorm 3), 12 March (snowstorm 4), and 19 and 20 March (snowstorm 5). Our study days began at 0000 UTC and ended at 2359 UTC. Daily precipitation collections were performed by Cheyenne NWS and CoCoRaHS observers at 0700 and 1400 UTC, respectively.

### a. Surface site

The focus of our study is a surface site located 25 km northwest of the Cheyenne NWS radar. The site (41°15'40"N, 105°03'52"W) is located on the eastern flank of the north-to-south-oriented Laramie Range and is surrounded by a treeless shortgrass prairie. With the exception of one residence, 30 m to the south of the site, there are no buildings within 1.2 km. Automated observations made at the site included snow rate, temperature, and wind speed from the Hotplate precipitation sensor TPS-3100 (Rasmussen et al. 2011; Yankee Environmental Systems, Inc.) and temperature, relative humidity, and wind speed from a Vaisala, Inc., weather station WXT510, hereinafter referred to as the "Vaisala." Data from these sensors were ingested once per second (1-Hz sampling) on a custom-built data system. Throughout this work, "altitude" is reported relative to sea level and "height" is reported relative to either the surface site (2093-m altitude) or the radar's antenna (1886-m altitude).

### b. Hotplate

The Hotplate consists of two vertically stacked 13-cm (diameter) circular plates mounted on a pedestal (Rasmussen et al. 2011). Control circuitry and resistive heating elements are designed to maintain the temperature of the Hotplate's top and bottom surfaces at approximately 75°C. Heat is lost from both surfaces

through ventilation. In the case of the top plate, a fraction of the electrical heating goes into melting and evaporation of snowfall. The difference between the electrical power provided to the two plates is used to compute  $S$ . Both a 1-min and a 5-min running average of  $S$  are formulated by the Hotplate's microprocessor. These averages are constructed using the 60 previous 1-Hz samples (1-min average) or using the 300 previous 1-Hz samples (5-min average). If the value of the 5-min average exceeds the threshold  $0.25 \text{ mm h}^{-1}$ , a provisional snow rate is stored as the 1-min average; otherwise, the provisional snow rate is stored as  $0 \text{ mm h}^{-1}$ . The provisional rate is divided by a wind speed-dependent catch efficiency, and this corrected snow rate is output to the data system once per second. Our Hotplate was purchased from Yankee Environmental Systems (Turners Falls, Massachusetts) in 2005 and utilized the firmware version 2.6.

We evaluated the uncertainty of the Hotplate-derived precipitation intensity, and the time response of the Hotplate, by randomly distributing uniform-sized water drops (2-mm sphere equivalent diameter) on the top plate surface. The mass flow rate of the water that produced the drops was steady and was measured with an accuracy of  $\pm 5\%$ . In these laboratory studies the flow rates of the water were equivalent to precipitation intensities between  $1.0$  and  $2.4 \text{ mm h}^{-1}$ . The mean absolute difference of the Hotplate-reported intensity, when compared with our standard, is  $0.03 \text{ mm h}^{-1}$ . The laboratory tests also revealed that the Hotplate can respond to the onset of precipitation in  $135 \text{ s}$  (Wolfe 2007).

During daytime, ambient temperature values reported by the Hotplate were typically  $2^\circ\text{C}$  higher than those reported by the Vaisala sensor. Temperature values reported by the Vaisala were used in this analysis. The Vaisala and Hotplate wind speeds were compared over each of the study days and agreed to within  $\pm 20\%$ .

### c. CoCoRaHS observations

We utilized precipitation observations from 12 CoCoRaHS observers. The selection of the 12 was based on their location; all of these stations are located east of the Laramie Range divide and within 25 km of the Cheyenne NWS radar. Table 1 has the CoCoRaHS 24-h accumulations, expressed as a liquid-equivalent depth, and air/ice densities. Both quantities are based on sampling performed at 1400 UTC. The densities were derived as the density of water ( $1000 \text{ kg m}^{-3}$ ) multiplied by the ratio of the liquid-equivalent depth and the corresponding snow-depth increment. Because the CoCoRaHS sampling is at 1400 UTC and the eight study days extend from 0000 to 2359 UTC, only six of our eight study days are available in the CoCoRaHS record. The CoCoRaHS observers used the same manual precipitation

TABLE 1. CoCoRaHS data.

Start time and date	CoCoRaHS liquid-equivalent depth (mm)*	CoCoRaHS density ( $\text{kg m}^{-3}$ )**
1400 UTC 15 Feb	$11.4 \pm 4.1$	$60 \pm 20$
1400 UTC 8 Mar	$7.3 \pm 3.3$	$90 \pm 50$
1400 UTC 10 Mar	$2.8 \pm 1.5$	$60 \pm 30$
1400 UTC 11 Mar	$5.0 \pm 2.2$	$90 \pm 30$
1400 UTC 18 Mar	$7.2 \pm 1.9$	$80 \pm 30$
1400 UTC 19 Mar	$11.3 \pm 5.4$	$110 \pm 60$

\* Average of liquid-equivalent depths (24-h accumulations) from the CoCoRaHS observers. Reports from 12 CoCoRaHS observers were used to evaluate the average. Gauges used by the 12 observers were located within 25 km of the Cheyenne NWS Office, and each observer reported a nonzero liquid-equivalent depth for the six days. Also reported is the standard deviation of the liquid-equivalent depth.

\*\* Air/ice densities evaluated as the density of water ( $1000 \text{ kg m}^{-3}$ ) multiplied by ratio of the liquid-equivalent depth and the corresponding snow-depth increment. Also reported is the standard deviation of the average.

gauge (unshielded) and the same techniques for determining the liquid-equivalent and snow depths. We analyze the CoCoRaHS accumulations in section 5d.

Only 7 of the 72 air/ice density measurements are indicative of graupel produced by riming [density greater than  $120 \text{ kg m}^{-3}$ ; Judson and Doesken (2000)]. Another 51 are smaller than  $120 \text{ kg m}^{-3}$  (averages and standard deviations are provided in Table 1), and the remaining density values are not available either because the snow-depth increment was not reported or because it was negligible. The latter is presumed to be the result of wind removing snow from the measurement location at a rate comparable to its deposition from the atmosphere.

### d. Weather Surveillance Radar-1988 Doppler

Radar reflectivity measurements were acquired by the Cheyenne Weather Surveillance Radar-1988 Doppler (WSR; Crum et al. 1993). The WSR transmits and receives horizontally polarized radiation at a wavelength of 10.7 cm. Microwave energy returned to the WSR can have a component, referred to as clutter, that does not originate from meteorological phenomena. The effect of clutter was minimized, prior to archival of the level-II data, by invalidating reflectivity values associated with Doppler velocity magnitudes smaller than  $1.75 \text{ m s}^{-1}$  (Ice et al. 2007). Chrisman and Ray (2006) describe the filter that was used for this data invalidation. We analyze the level-II WSR data.

We used four criteria to select values of  $Z_e$  that were correlated with snow rate. First, only retrievals from the two range gates closest to the surface site were selected.

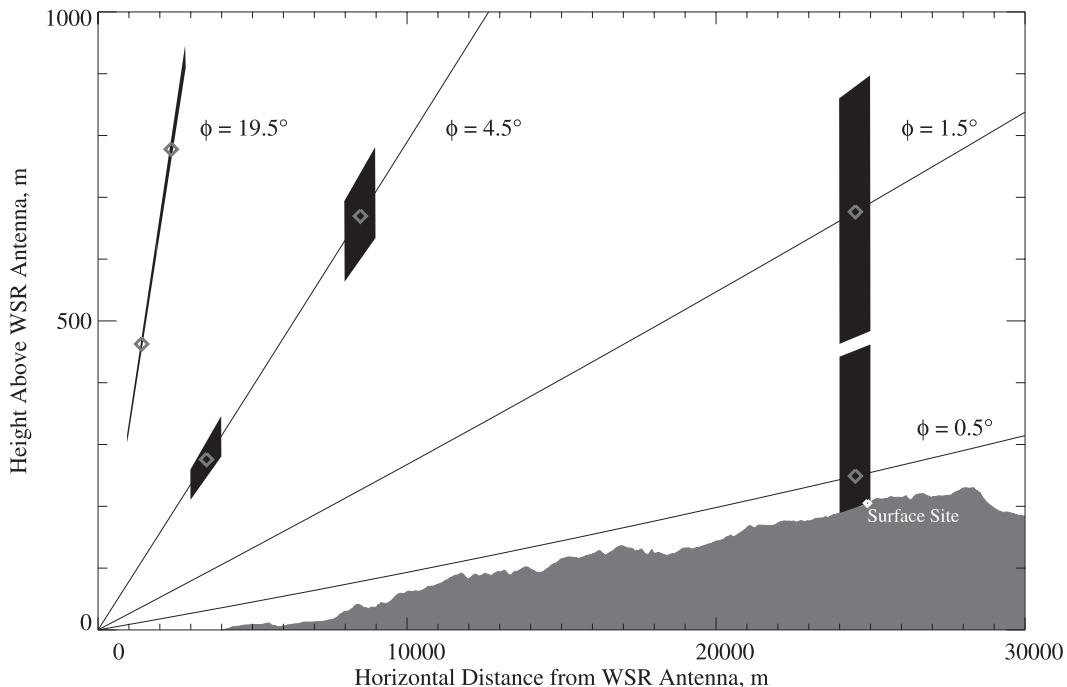


FIG. 1. A height–distance cross section along the 299° radial connecting the WSR and the surface site. Ray paths were constructed by integrating Eq. (3.19) of Battan (1973) under the assumption that the vertical gradient of the index of refraction is a constant ( $dn/dz = -3 \times 10^{-8} \text{ m}^{-1}$ ). Illustrated are range gates along the highest tilt angle of VCP-21 (19.5°), range gates along the highest tilt angle of VCP-32 (4.5°), and the two range gates over the surface site. Midpoints of the gates are indicated by a gray open diamond, and the gate is black (see text and Table 2 below for details).

These range gates are seen lying along ray paths defined by 0.5° and 1.5° radar tilt angles at the right edge of Fig. 1. Second, to avoid Bragg scatter (Knight and Miller 1993; Kollias et al. 2007), only reflectivities that are larger than  $10 \text{ mm}^6 \text{ m}^{-3}$  were selected. Further justification for this  $Z_e$  threshold is provided in section 4c. Third, we matched a retrieval validated by the first two criteria to a particular snow rate. The time interval that was searched for the matching snow rate extended 60 s backward from the time of the radar measurement. From the 60 possible matches, the nonzero value closest to the radar measurement was selected. This selection acknowledges the signal averaging performed by the Hotplate microprocessor (section 2b). Fourth, if none of the snow-rate matches exceeded zero, then the  $Z_e$  value was eliminated.

In sections 5b and 5d, we apply a particular  $Z_e$ – $S$  relationship, developed in section 5a, to reflectivities in excess of  $10 \text{ mm}^6 \text{ m}^{-3}$  and output a radar-derived snow-rate time series. The time resolution of the latter is either 645 or 363 s, depending on how the radar was scanned (section 4). Also presented are time series of the radar-derived liquid-equivalent accumulation. These were obtained by summing the product of the radar-derived snow rate multiplied by the interval of time between reflectivities. To avoid unwarranted extrapolation

of the radar measurements, time intervals greater than 645 s were invalidated, and the associated accumulation increments were excluded from the radar-derived accumulation.

#### e. Synchronization

We synchronized the Hotplate clock and the surface-site data system clock to a reference on 1 February 2006. Our comparison of the two clocks revealed a mismatch that never exceeded 100 s during February and March of 2006. The data system clock was chosen for synchronizing the surface measurements to the WSR. In addition to the likely drift of the time reference we chose for the surface site, the surface and radar datasets are misaligned because of the time it takes for a snow particle to fall from the radar range gate to the ground. The maximum particle fall distances, from the 0.5° and 1.5° range gates, are 300 and 700 m, respectively (Fig. 1). Assuming a representative fall speed for a crystal with branched structure [ $0.5 \text{ m s}^{-1}$ ; e.g., Fig. 6 in Mitchell and Heymsfield (2005)] and no vertical air motion, the time mismatch between the WSR and surface-site measurements could be as large as 1400 s. In our processing of the WSR and surface measurements, we tested mismatches as large as 1500 s, but these perturbations did not substantially improve the  $Z_e$ – $S$  correlation.

f. Blockage

Figure 1 demonstrates that approximately 50% of the 0.5° transmission, along the 299° radial connecting the WSR and the surface site, is blocked by the terrain. In contrast, the 1.5° transmission is not affected by beam blockage. Partial blockage of the former suggests that reflectivities retrieved from that ray path are negatively biased. The blockage translates to a shift of  $-3$  dB $Z_e$  when expressed in decibels (Smith 1998). This issue is discussed in section 4b.

3. Linkage between theory and observation

Reflectivity–snowfall relationships, examined in detail in section 5, are commonly expressed in terms of a power law:

$$Z_e = \alpha S^\beta, \tag{1}$$

where  $Z_e$  is the equivalent radar reflectivity factor and  $S$  is the snowfall rate (expressed as the liquid equivalent per unit time). The coefficients  $\alpha$  and  $\beta$  are generally determined by correlating values of  $Z_e$  and  $S$  (either observed directly or computed from measurements of the particle size distribution). By convention,  $Z_e$  and  $S$  are expressed in millimeter to the sixth power per cubic meter ( $\text{mm}^6 \text{m}^{-3}$ ) and millimeter per hour, respectively. We adopt that convention in sections 5 and 6, but the theoretical relationships developed here have all quantities expressed with Système International (SI) base units (meter, kilogram, and second).

Rasmussen et al. (2003) present a theory describing how  $\alpha$  and  $\beta$  vary with properties of precipitation within a radar viewing volume. Here, we summarize their development for snow particles with a temperature of less than 0°C, extend their result, and demonstrate a theoretical connection between  $\alpha$  and particle concentration. The latter is the basis for the hypothesized connection between  $\alpha$  and temperature. Throughout this discussion we symbolize a snow particle’s characteristic dimension as  $D$  and assume that the particles have spherical shape (Smith 1984; Rasmussen et al. 2003).

There are five parameterizations and related assumptions in the development of Rasmussen et al.: 1) The snow-particle size distribution is an exponential function of the form  $n(D) = n_o \exp(-\lambda D)$ , where  $n_o$  is the intercept and  $\lambda$  is the slope. 2) The particle’s air/ice density  $\rho_s$  is described as  $\rho_s = \Omega/D$ , where  $\Omega$  is a parameter that we take to be a constant (Brown and Francis 1995; Pokharel and Vali 2011). 3) The particle fall speed  $V_i$  is a constant. This is consistent with observations demonstrating that for snow particles with

minimal riming the  $V_i$ – $D$  relationship has a small slope for  $D > 1 \times 10^{-3}$  m (Mitchell and Heymsfield 2005). 4) The microwave scattering is described by Rayleigh theory with the snow particle’s dielectric factor scaling as  $\rho_s^2$ . With these, Rasmussen et al. (2003) derived the following  $Z_e$ – $S$  relationship:

$$Z_e = \left( 22.2 \frac{|K_i|^2 \rho_w^{5/3} \Omega^{1/3}}{|K_w|^2 \rho_i^2 V_i^{5/3} n_o^{2/3}} \right) S^{5/3} \text{ (m}^6 \text{ m}^{-3}\text{)}, \tag{2}$$

where  $|K_i|^2$  and  $|K_w|^2$  are the dielectric factors for ice and water (0.18 and 0.93, respectively, at S band) and  $\rho_i$  and  $\rho_w$  are the ice and water densities ( $920$  and  $1000 \text{ kg m}^{-3}$ ).

We extend Eq. (2) by noting that its derivation starts with separate developments for  $Z_e$  and  $S$ , leading to two equations, the first with  $Z_e$  proportional to the fourth moment of  $n(D)$  and the second with  $S$  proportional to  $n(D)$ ’s second moment. We note that these moment relations differ from that for rain. This results because Rasmussen et al. formulated  $Z_e$  and  $S$  in terms of ice particle size and not melted diameter, because they parameterized the air/ice density as  $\rho_s = \Omega/D$ , and because an ice particle’s dielectric factor is proportional to the square of the air/ice density. As in Rasmussen et al. but for the zeroth moment of  $n(D)$ , we apply the recurrence relation for moments of an exponential function [e.g., see Eq. (10.11) in Rogers and Yau (1989)] and derive an alternate form for the  $Z_e$ – $S$  relationship:

$$Z_e = \left( 21.9 \frac{|K_i|^2 \rho_w^2}{|K_w|^2 \rho_i^2 V_i^2 N} \right) S^2 \text{ (m}^6 \text{ m}^{-3}\text{)}. \tag{3}$$

Here,  $N$  is the zeroth moment of the size distribution, that is, the total concentration integrated over all particle sizes. We see that  $\Omega$  cancels out of this  $Z_e$ – $S$  relationship and that  $\alpha$  [the first term on the right side of Eq. (3)] is a function of precipitation properties  $N$  and  $V_i$ .

Previous studies of snow have revealed correlations among the size distribution’s moments. Examples include the work of Gunn and Marshall (1958), whose parameterizations reveal that  $N$  and ice water content (IWC) are negatively correlated, and Braham (1990), who presented positively correlated values of  $N$  and IWC. With an assumption that the product of IWC and a constant  $V_i$  is a reliable estimate of  $S$ , these two  $N$ –IWC correlations imply that, in Eq. (3), the index on  $S$  can vary by  $\pm 25\%$ . In this work, we assume  $\beta = 2$ , consistent with our theoretical development, and derive  $\alpha$  by fitting paired measurements of  $Z_e$  and  $S$ . Last, we note that our  $\beta = 2$  assumption is consistent with most

values presented by Rasmussen et al. (their Table 1) and with determinations of  $\beta$  derived from paired WSR and precipitation gauge measurements (Super and Holroyd 1998).

Equation (3) indicates that  $\alpha$  should vary inversely proportional to  $N$ . This ignores the fall speed dependence seen in Eq. (3) and the fact that for a prescribed  $D$  a rimed particle has a fall speed that is severalfold larger than that of an unrimed particle (e.g., Fig. 9.7 in Rogers and Yau 1989). Our analysis of air/ice densities, based on the CoCoRaHS sampling (section 2c), is consistent with snow particles that were not produced by riming.

Ice crystal nucleation, or crystal multiplication, is the starting point for precipitation development through deposition, aggregation, or riming. Lagrangian investigations of depositional growth, made by an aircraft flying a spiral descent such that the aircraft descends at the fall speed of the snow particles, demonstrate that the slope  $\lambda$  of the exponential size distribution function remains approximately constant while the intercept  $n_o$  increases downward (Lo and Passarelli 1982). This behavior is expected for a size distribution evolving through the combined processes of crystal production with growth by vapor diffusion.

In contrast, the agglomeration of individual ice crystals into aggregates transfers mass from small particles to larger ones, thereby reducing the concentration of small particles (single ice crystals) and increasing the abundance of larger snow particles (the aggregates). As a result, both  $\lambda$  and  $n_o$  decrease (Lo and Passarelli 1982; Gordon and Marwitz 1986). When riming is minimal, aggregate fall speed  $V_t$  is fairly insensitive to size, only tripling over the interval  $1 \times 10^{-4} \leq D \leq 1 \times 10^{-2}$  m, and for larger  $D$  the fall speed is predicted to decrease with increasing size (Mitchell and Heymsfield 2005). Because aggregation conserves mass while leaving  $V_t$  relatively unchanged,  $S$  is also unchanged, or decreases ( $D > 1 \times 10^{-2}$  m) while  $Z_e$  increases because of its strong dependence on  $D$  (Smith 1984).

Examination of the individual crystals that compose an aggregate demonstrates that dendritic shapes are common (Ohtake 1970; Fujiyoshi and Wakahana 1985). A reanalysis of the Lo and Passarelli (1982) data indicates that crystals with branched structure (i.e., sector plates and dendrites) are favorable for aggregation (Mitchell 1988). The thermodynamic conditions necessary for the maintenance of branched structures are temperature between  $-19^\circ$  and  $-11^\circ\text{C}$  and water saturation (Rogers and Yau 1989). Given that we do not see much evidence for riming (section 2c) and that droplet size within upslope snowstorms is often too small to produce significant riming (Boatman and Reinking 1984; Wang and Ji 2000), we conclude that, of the three

plausible precipitation processes (riming, aggregation, and vapor deposition), aggregation and vapor deposition are dominant. In section 5c we will demonstrate, from an analysis of a subset of our measurements, that an even more restrictive interpretation of the dominating precipitation process is possible and that the  $\alpha$ - $N$  relationship [Eq. (3)] can be interpreted as an  $\alpha$ - $T$  relationship.

#### 4. Radar measurements

In this section, we compare reflectivities retrieved from range gates positioned over the surface site along ray paths defined by the  $299^\circ$  radial and tilt angles of  $0.5^\circ$  and  $1.5^\circ$ . Figure 1 shows the ray paths, the range gates (black), and the range gate midpoints (gray diamonds). In addition, we evaluate retrievals from range gates lying along ray paths defined by the largest possible tilt angles ( $4.5^\circ$  and  $19.5^\circ$ ). The  $1.5^\circ$ ,  $4.5^\circ$ , and  $19.5^\circ$  ray paths are not expected to be biased by beam blockage, but underestimation is expected for reflectivities obtained from the  $0.5^\circ$  gate. We examine this by assimilating retrievals from  $0.5^\circ$  and  $1.5^\circ$  and formulating a low-level vertical reflectivity gradient and by comparing that gradient with one obtained from retrievals made along either the  $4.5^\circ$  or  $19.5^\circ$  ray path.

To facilitate these analyses, we approximate the WSR range gates as cylinders with orientation, relative to horizontal, defined by the radar's tilt angle and by a selected value of the vertical gradient of the index of refraction ( $dn/dz = -3 \times 10^{-8} \text{ m}^{-1}$ ). The refraction gradient was based on an average potential temperature gradient ( $\langle d\theta/dz \rangle$ ) that we derived by analyzing NWS radiosonde data acquired over Rapid City, South Dakota (eight study days). For the 750–500-hPa layer, we derived an average potential temperature gradient  $\langle d\theta/dz \rangle = 5 \times 10^{-3} \text{ K m}^{-1}$ . At altitudes lower than 750 hPa, we took the average potential temperature gradient to be  $\langle d\theta/dz \rangle = 15 \times 10^{-3} \text{ K m}^{-1}$ . The latter is consistent with postfrontal cross sections reported for upslope snowstorms by Boatman and Reinking (1984). Water-saturated conditions were assumed for all levels. Within the two layers, we found the refractive index gradient to vary between  $-4 \times 10^{-8}$  and  $-2 \times 10^{-8} \text{ m}^{-1}$ . We note that even the smaller of these limits is substantially larger than  $dn/dz = -16 \times 10^{-8} \text{ m}^{-1}$ , the value that produces downward bending of a radar transmission (Battan 1973). The dimensions of the cylinders are determined by the radar's operating mode (Crum et al. 1993; Miller et al. 1998), and, for the level-II data that we analyze, only two operating modes are evident. These are referred to as volume coverage patterns 21 (VCP-21) and 32 (VCP-32). Table 2 presents the

TABLE 2. Radar range gates.

Location of range gate	VCP	Tilt angle (°)	Range gate length (m) <sup>a</sup>	Range (m) <sup>b</sup>	Height (m) <sup>c</sup>	Indicated height (m) <sup>d</sup>
Over surface site	32 or 21	0.5	1000	24 510	250	300
Over surface site	32 or 21	1.5	1000	24 520	680	700
Close to WSR	32	4.5	1000	3520	280	300
Close to WSR	32	4.5	1000	8520	670	700
Close to WSR	21	19.5	1000	1500	460	300
Close to WSR	21	19.5	1000	2510	780	700

<sup>a</sup> Although the range gate length depends on the duration of the transmitted radar pulse, which varies with VCP, we use the level-II data, which are regridded to a range gate length of 1000 m (Crum et al. 1993).

<sup>b</sup> Distance from WSR antenna to the range gate center. The ray path is derived by integrating Eq. (3.19) of Battan (1973) while assuming that the vertical gradient of the index of refraction is a constant ( $dn/dz = -3 \times 10^{-8} \text{ m}^{-1}$ ). Values are reported with a precision of  $\pm 10$  m.

<sup>c</sup> Height of the center of the range gate relative to the altitude of the WSR antenna. Values are reported with a precision of  $\pm 10$  m.

<sup>d</sup> The height used to label Fig. 2, below. Gate heights are classified into two categories, 1) those with height comparable to the 0.5° gate (300 m) and 2) those with height comparable to the 1.5° gate (700 m).

dimensions of the range gates, and descriptions of the coverage patterns are in Miller et al. (1998).

Figures 2a–d contain all of the  $Z_e$  values available for the six range gates (Table 2) and for the eight study days. Four of the six gates are located along the ray paths defined by the largest radar tilt angle. Table 2 shows that the heights of these “close to WSR” range gates match, to within  $\sim 200$  m, the height of gates positioned over the surface site. This correspondence between gate height close to the WSR and that over the surface site is also evident in Fig. 1. For clarity, points from two of the days in Fig. 2a are repeated in Fig. 2c. In Fig. 2d we present a subset from Fig. 2b consisting of “over surface site” retrievals that are coincident with detectable snow rate as stipulated by the third selection criterion described in section 2d. These four plots are discussed in the next three sections.

*a. Vertical gradient of the reflectivity*

The data points in Figs. 2a–d are color coded by day with retrievals on three of the eight days using VCP-21 (11, 19, and 20 March) and the other five using VCP-32. We start our analysis of the vertical reflectivity gradient with

$$Z_{e,Y} = aZ_{e,X}. \tag{4a}$$

Here,  $Z_{e,Y}$  is the reflectivity factor from the larger of two heights and  $Z_{e,X}$  is the reflectivity from the lower height. By taking the logarithm of Eq. (4a), we transform the reflectivities to their decibel equivalent and arrive at the equation used for diagnosing the vertical reflectivity gradient:

$$\text{dB}Z_{e,Y} = 10 \log_{10}(a) + \text{dB}Z_{e,X}. \tag{4b}$$

In this format, an upward-decreasing reflectivity has a value of  $10 \log_{10}(a)$  that is smaller than zero [i.e.,  $a < 1$

in Eq. (4a)]. Values of  $10 \log_{10}(a)$  were derived by linear least squares fitting of the decibel values of  $Z_{e,Y}$  (plotted on the Y axis) and  $Z_{e,X}$  (plotted on the X axis) and are presented with their statistical uncertainty in the lower-right corners of Figs. 2a–d. Because of the way we have defined  $10 \log_{10}(a)$ , its numerical sign is the same as that of the low-level vertical reflectivity gradient  $dZ_e/dz$ . Hence, negative values of  $10 \log_{10}(a)$  correspond to negative values of  $dZ_e/dz$  (upward-decreasing reflectivity), and vice versa. In the plotting in Figs. 2a–d, the scenario of reflectivity decreasing upward has a fit line parallel to and below the one-to-one line, and the opposite is the case for reflectivity increasing upward. The fit lines are not shown in Figs. 2a–d.

Figure 2a is a plot of data collected close to the WSR, along ray paths defined by the largest tilt angle. It shows three days (16 February and 19 and 20 March) with negative values of  $10 \log_{10}(a)$  and thus larger reflectivity (on average) associated with the lower of the two paired range gates (i.e.,  $dZ_e/dz$  is negative). The negative  $Z_e$  vertical gradient implied by these measurements is consistent with analyses of snowstorms at Denver, Colorado (Super and Holroyd 1998), and Cheyenne (Matrosov et al. 2008). The former authors speculated that the occurrence of  $dZ_e/dz < 0$  is indicative of particle growth increasing with fall distance, even at low altitudes. In contrast, the 8 and 10 March data exhibit positive  $10 \log_{10}(a)$  and thus a positive  $dZ_e/dz$ . A positive reflectivity gradient is also indicated by the value  $10 \log_{10}(a) = 1.5$  in the 11 March data, although the statistical uncertainty is relatively large on this day. In an analogous way, on 15 February and 12 March the magnitude of  $10 \log_{10}(a)$  is comparable to its statistical error. WSR data from two days, one with evidence for a negative  $Z_e$  vertical gradient (19 March) and one showing the opposite (8 March), are repeated in Fig. 2c. In both

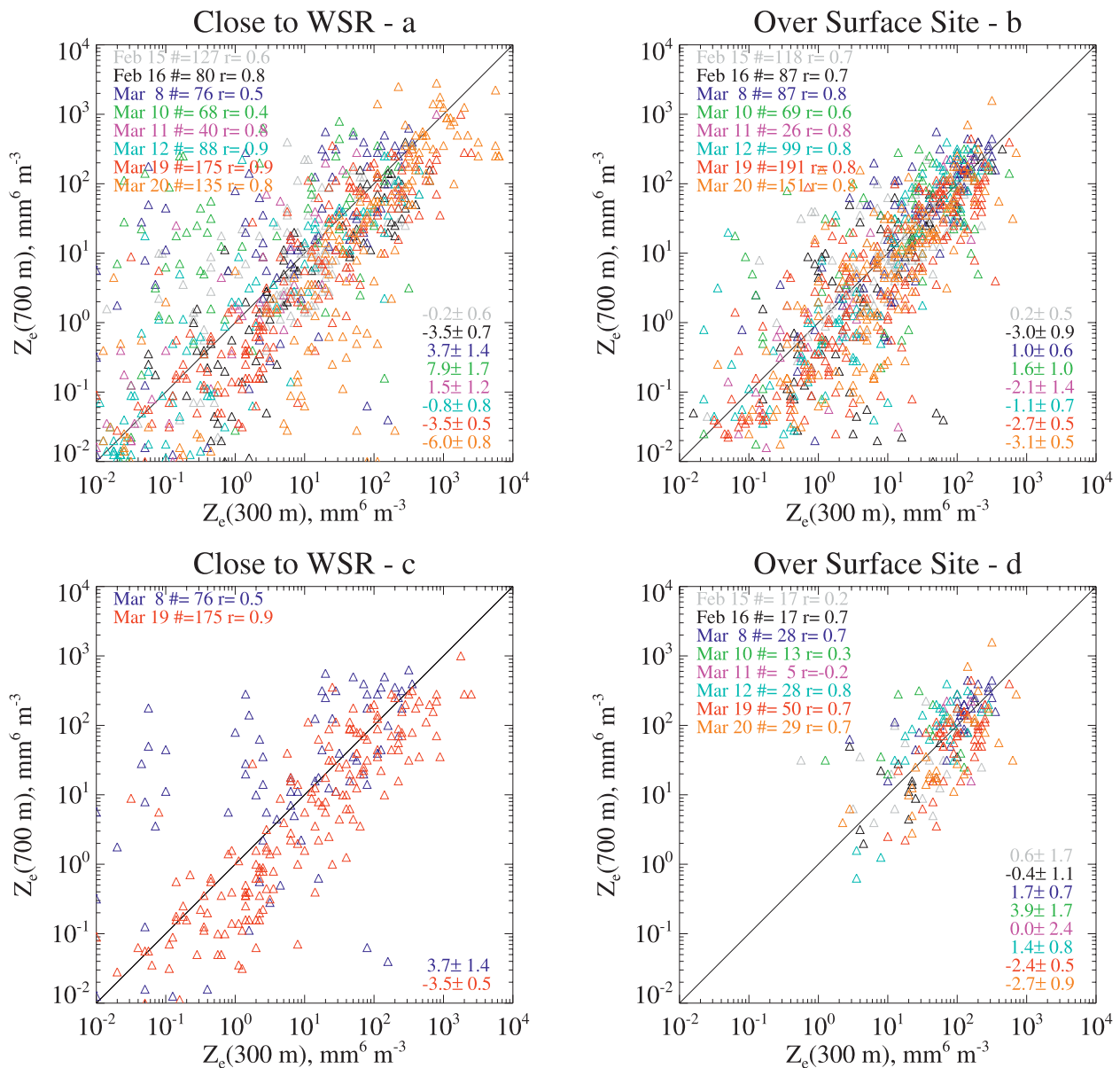


FIG. 2. Scatterplots of radar reflectivity retrieved close to the WSR and over the surface site. See Table 2 for range-gate specifications. Shown are (a)  $Z_e$  close to the WSR, along ray paths defined by the maximum tilt angle, and (b)  $Z_e$  over the surface site, along ray paths defined by the tilt angles 1.5 and 0.5°. (c) As in (a), but repeating only the data from 8 and 19 March. (d) As in (b), but for radar retrievals coincident with Hotplate  $S > 0.25 \text{ mm h}^{-1}$ . In the lower right of all panels is  $10 \log_{10}(a)$  and its statistical uncertainty. In the upper left of all panels is the number of points (labeled as #) and the Pearson product moments  $r$ .

Fig. 2c and Fig. 2a, it is evident that the variability of the data about the one-to-one line is larger for  $Z_e$  values that are less than  $10 \text{ mm}^6 \text{ m}^{-3}$ .

### b. Clutter and blockage

The prior discussion indicated that on three days the reflectivity decreased upward. Our determination of the reflectivity gradient was based on retrievals from the close-to-WSR range gates (i.e., from gates at a range of

less than 10 km; see Table 2). Despite the application of clutter invalidation (section 2d), there is concern that retrievals from such a short range can be contaminated by clutter (Melnikov et al. 2009). In that scenario we expect retrievals from the lower of the two range gates to be more strongly biased by residual ground clutter. Hence, our attribution of the sign of the reflectivity gradient to meteorological conditions (i.e., snow-particle growth) could be incorrect. When expressed in decibels,

the average enhancement at the lower of the two altitudes is 3.5, 3.5, and 6.0 dB for 16 February and 19 and 20 March, respectively (Fig. 2a). Arguing for our conclusion that these low-level reflectivity enhancements are of meteorological origin are results presented in Fig. 2b. Here, we present scatterplots and the fit coefficient from measurements retrieved over the surface site. For 16 February and 19 and 20 March, it is evident that the value of  $10 \log_{10}(a)$  has the same sign in Figs. 2a and 2b, but a quantitative comparison reveals that  $10 \log_{10}(a)$  is larger in Fig. 2b. We acknowledge that this increase could be a consequence of blockage of the  $0.5^\circ$  ray path over the surface site or could be because the  $Z_e$  from the  $4.5^\circ$  or the  $19.5^\circ$  ray paths (at the lower of the two range gate heights) may be biased by residual ground clutter. Distinguishing between these two possibilities is difficult, but in the following paragraphs we present measurements that are consistent with the idea that the sign of  $10 \log_{10}(a)$ , and thus the sign of  $dZ_e/dz$ , are a response to meteorological conditions.

Table 3 presents averages of a quantity derived from measurements made by the Vaisala at the surface site. The Vaisala relative humidity (RH) measurements were averaged over samples that satisfy the Hotplate condition  $S > 0.25 \text{ mm h}^{-1}$  (section 2b). The number of samples that satisfy the condition is shown. It is evident that between 5% (11 March) and 30% (8 March) of the RH measurements were coincident with  $S > 0.25 \text{ mm h}^{-1}$ . Values presented in the third column in Table 3 are averages of the selected relative humidity values scaled by the ratio of the water saturation vapor pressure divided by the ice saturation vapor pressure. This quantity is commonly known as the ice saturation ratio. Values of the ice saturation ratio in excess of unity are necessary for snow-particle growth by deposition. Table 3 demonstrates that ice saturation was exceeded, on average, on the three days that exhibited a negative reflectivity gradient (16 February and 19 and 20 March). Thus, conditions were favorable for the growth of particles close to the ground, but we cannot distinguish the importance of growth by deposition versus that by aggregation. For the two days with both a statistically robust and positive reflectivity gradient (8 and 10 March) there is some evidence for low-level particle sublimation. This is evident in the humidity variability, which is larger on 8 and 10 March when compared with the three previously mentioned days. Overall, results from five of the eight study days are consistent with the conclusion that the low-level reflectivity gradient was influenced by particle growth (through deposition or aggregation; 16 February and 19 and 20 March) and particle sublimation (8 and 10 March).

TABLE 3. Ice saturation ratio and temperature. Here, NA indicates that Vaisala data are not available for that day.

Date	No. of data points <sup>a</sup>	Ice saturation ratio <sup>b</sup>	Temperature ( $^\circ\text{C}$ ) <sup>c</sup>
15 Feb	10 913	NA	$-9 \pm 1$
16 Feb	12 313	$1.05 \pm 0.01$	$-13 \pm 2$
8 Mar	19 636	$1.01 \pm 0.03$	$-4 \pm 1$
10 Mar	8388	$1.00 \pm 0.05$	$-12 \pm 1$
11 Mar	2607	$0.96 \pm 0.14$	$-11 \pm 1$
12 Mar	16 933	$1.02 \pm 0.01$	$-8 \pm 1$
19 Mar	16 788	$1.01 \pm 0.01$	$-3 \pm 1$
20 Mar	11 082	$1.04 \pm 0.01$	$-8 \pm 2$

<sup>a</sup> The number of 1-Hz samples that satisfy the Hotplate condition  $S > 0.25 \text{ mm h}^{-1}$ .

<sup>b</sup> Computed from the measurement of RH (expressed as a fraction) and temperature  $T$ . The ice saturation ratio is  $\text{RH} \times e_w(T)/e_i(T)$ , where  $e_w(T)$  is the saturation vapor pressure over liquid water and  $e_i(T)$  is the saturation vapor pressure over ice. Values reported in this column are the ice saturation ratio, averaged over samples that satisfy the Hotplate condition  $S > 0.25 \text{ mm h}^{-1}$ . The standard deviation of the average is also reported.

<sup>c</sup> Temperature and its standard deviation for 1-Hz samples that satisfy the Hotplate condition  $S > 0.25 \text{ mm h}^{-1}$ .

### c. Reflectivities coincident with snowfall

As was mentioned above (section 4), points from Fig. 2b that were coincident with detectable snow at the surface site ( $S > 0.25 \text{ mm h}^{-1}$ ) were used to construct Fig. 2d. We note that the number of selected points is smaller, by a factor of approximately 4. This may demonstrate that the WSR is more sensitive to low-level snowfall than the Hotplate is, consistent with the radar's enormous footprint relative to the area of the Hotplate, but it could also be that a fraction of the deselected points were a consequence of the radar responding to nonmeteorological phenomena. It is also apparent that the  $S > 0.25 \text{ mm h}^{-1}$  selection has eliminated most of the  $Z_e$  values that are smaller than  $10 \text{ mm}^6 \text{ m}^{-3}$ . Because retrievals at  $Z_e < 10 \text{ mm}^6 \text{ m}^{-3}$  exhibit more variability (e.g., Fig. 2b) and can include a disproportionate fraction of values that are influenced by Bragg scatter (Knight and Miller 1993; Kollias et al. 2007) and residual ground clutter (Miller et al. 1998; Melnikov et al. 2009), we have chosen to restrict the following analyses to reflectivities that are larger than  $10 \text{ mm}^6 \text{ m}^{-3}$ . According to our deduced  $Z_e$ - $S$  relationship (section 5a), this reflectivity threshold corresponds to  $S = 0.30 \text{ mm h}^{-1}$ .

### d. Echo-top height

In section 5c we use measurements of the snowstorm's echo-top height as a surrogate for the minimum cloud temperature. The method used to quantify the radar echo-top height is explained here. Using retrievals

from the 299° radial and along ray paths defined by the highest available tilt angle, a reflectivity profile was constructed. In a first step, we rejected profiles with a lowest-height reflectivity value of less than  $10 \text{ mm}^6 \text{ m}^{-3}$ . This check selects against low-level retrievals that result from either residual clutter or Bragg scatter. We then evaluated the profile of reflectivity until the highest gate with  $Z_e > 1 \text{ mm}^6 \text{ m}^{-3}$  is reached. The height of the gate immediately above the last gate with  $Z_e > 1 \text{ mm}^6 \text{ m}^{-3}$  was taken to be the echo-top height. Figure 3 presents the distribution of echo-top height for the five warmest and the three coldest of the eight study days. Implications of this result are discussed in section 5c.

## 5. Results

In this section we explain how the selected  $Z_e$ - $S$  pairs were correlated. The starting point is Eq. (1) with the value of  $\beta$  set equal to 2 (section 3). The statistical methods used to derive  $\alpha$  are described. Next, time series of surface site and radar measurements are presented, the temperature dependence of  $\alpha$  is examined, and the radar-derived 24-h accumulations are compared with an independent set of gauge measurements.

### a. Correlations

We used three statistical methods to calculate  $\alpha$  (see the appendix). The first minimizes the departure of  $Z_e$  from the line  $Z_e = \alpha_1 S^2$ , the second minimizes the departure of  $S^2$  from the line  $Z_e = \alpha_2 S^2$ , and the third minimizes the departure of  $\ln Z_e$  from the line  $\ln Z_e = \ln \alpha_3 + \ln S^2$ . Also presented in the appendix are the formulas used to evaluate statistical errors associated with the three fitted coefficients:  $\sigma_{\alpha_1}$ ,  $\sigma_{\alpha_2}$ , and  $\sigma_{\alpha_3}$ .

Figure 4 presents plots of  $Z_e$  versus  $S$  for the  $0.5^\circ$  (Fig. 4a) and the  $1.5^\circ$  (Fig. 4c) ray paths. The data pairs were selected by applying the four criteria discussed in section 2d, and selected values from all eight study days are plotted. Because the middle fit line (corresponding to  $\alpha_3$ ) is between the fit lines coming from the two other methods, we picked  $\alpha_3$  to represent the  $Z_e$ - $S$  relationship at Cheyenne. Values for  $\alpha_3$  in Figs. 4a and 4c are in good agreement. We average these to obtain an overall  $\alpha$  and use this in the following section and in section 5d. The value that we recommend is  $\alpha = 110 \text{ mm}^4 \text{ h}^2 \text{ m}^{-3}$ .

When quantified in terms of a Pearson product moment  $r$ , the correlations in Figs. 4a and 4c are  $r = 0.37$  and  $r = 0.22$ , respectively. These are significant correlations, with “ $p$  values” that are smaller than 0.05, but the magnitudes of  $r^2$  are small relative to unity. This demonstrates that, in practical application,  $Z_e$  combined with a  $Z_e$ - $S$  relationship is an incomplete descriptor of  $S$ . Because of this, we examine the temperature dependence

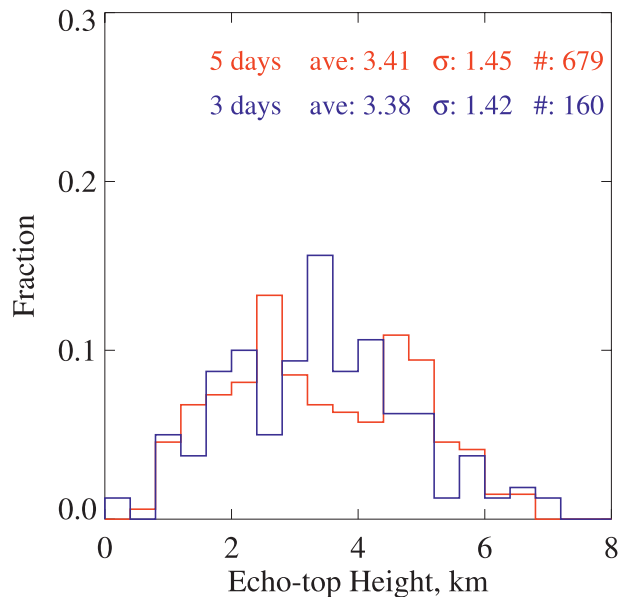


FIG. 3. Echo-top-height probability distribution functions derived from WSR measurements made on the eight study days. Red signifies heights selected from the five days with the warmest average surface-site temperature; blue signifies heights selected from the three days with the coldest average surface-site temperature. The legend presents the average echo-top height, the standard deviation  $\sigma$  of the distribution, and the number of valid vertical profiles (labeled as #).

of  $\alpha$  in section 5c. Further, we note that the  $Z_e$ - $S$  correlations are stronger when using the  $0.5^\circ$  reflectivities, possibly because the lower-height subset is better synchronized with the Hotplate.

The day-specific  $Z_e$ - $S$  correlations, obtained by grouping values acquired at both tilt angles ( $0.5^\circ$  and  $1.5^\circ$ ), were positive and statistically significant ( $p < 0.05$ ) on three of the eight study days. These are 19 March ( $r = +0.5$ ; number of points  $n = 85$ ), 12 March ( $r = +0.6$ ;  $n = 52$ ), and 20 March ( $r = +0.4$ ;  $n = 49$ ). Weaker correlations, all insignificant at  $p = 0.05$ , were evident on 15 February ( $r = +0.2$ ;  $n = 28$ ), 8 March ( $r = +0.1$ ;  $n = 58$ ), 10 March ( $r = -0.1$ ;  $n = 22$ ), and 11 March ( $r = +0.5$ ;  $n = 9$ ). The one study day with a  $Z_e$ - $S$  correlation that was negative and also significant ( $r = -0.4$ ;  $n = 34$ ;  $p = 0.01$ ) was 16 February. Because of their unusual behavior, data from 16 February are examined in greater detail in section 5b.

Figures 4b and 4d show the correlation between the radar-derived and Hotplate values of  $S$ . We see that the slopes of the  $y = ax$  fit lines (solid) are close to unity, indicating that on average the bias is small. Substantial variability is also apparent. The dashed lines in these two figures have 16% of the data pairs above them (upper dashed line) and 16% of the data pairs below them (lower dashed line). It is apparent that a factor-of-2 disagreement between a radar-derived snow rate and

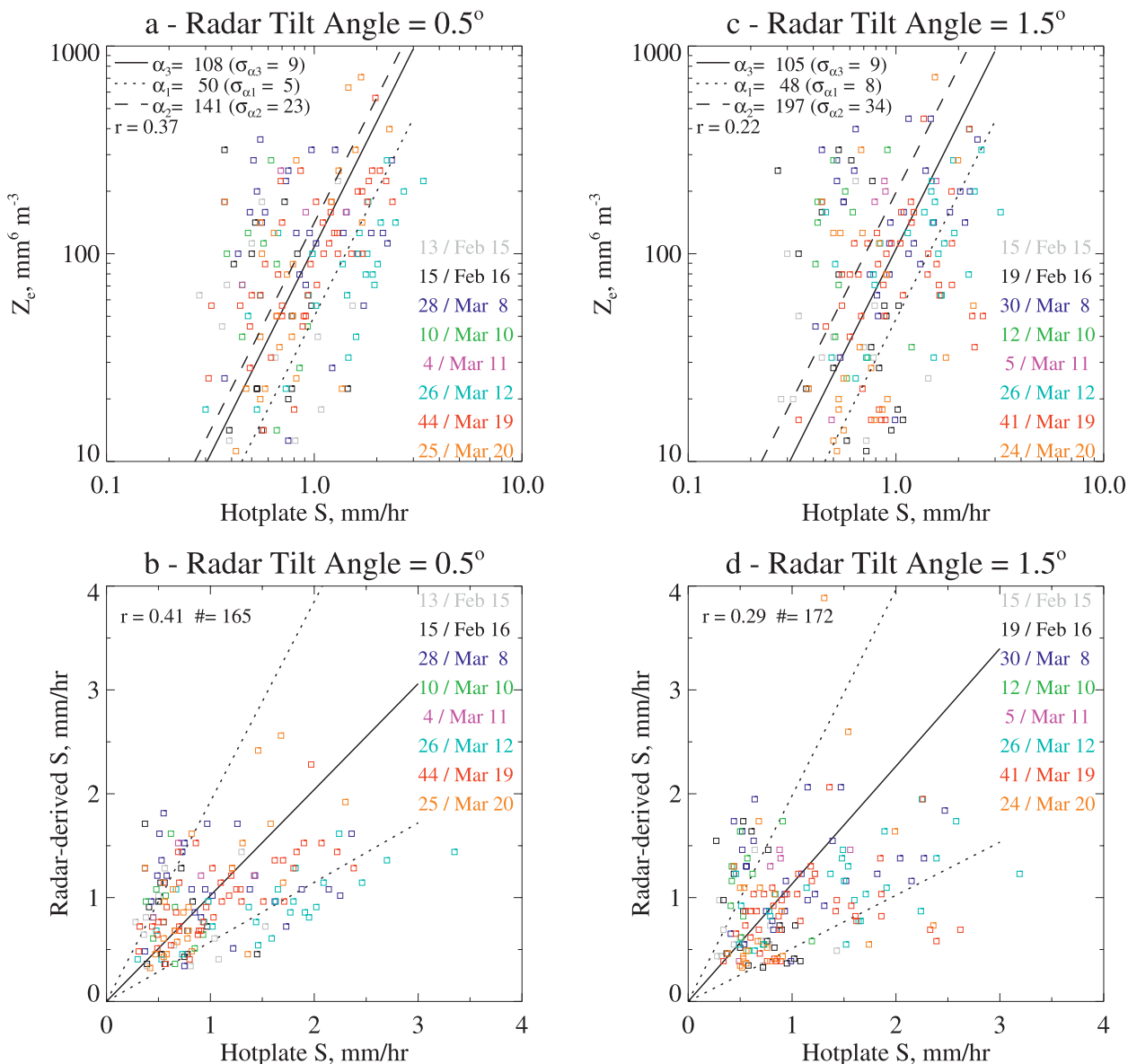


FIG. 4. (a) A  $Z_e$ -S scatterplot with radar reflectivities from the 0.5° ray path. Fit lines correspond to the three fitting methods (see the appendix), and values of the three fitted coefficients, their statistical errors, and the Pearson product moment  $r$  are presented in the upper-left corner. The number of points for each day is shown along the right margin. (b) Scatterplot of the radar-derived snow rate ( $\alpha = 108 \text{ mm}^4 \text{ h}^2 \text{ m}^{-3}$ ) on the basis of reflectivities from the 0.5° ray path vs the coincident Hotplate snow rate. Also shown is the Pearson product moment and the total number of points (labeled as #). (c) As in (a), but with reflectivity from the 1.5° ray path. (d) Scatterplot of the radar-derived snow rate on the basis of reflectivities from the 1.5° ray path vs the coincident Hotplate snow rate.

a Hotplate snow rate is not uncommon. Comparable variability is evident in a scatterplot of hour-averaged gauge snow rate and radar-derived snow rate presented by Super and Holroyd (1998, their Fig. 8).

*b. Time series*

Figures 5 and 6 contain surface-site and WSR measurements from 19 March and 16 February, respectively.

The time interval in both figures is 6 h. Of note, in Figs. 5c and 6c, is the occurrence of humidities in excess of ice saturation (both figures) and of humidities approaching water saturation on 19 March (Fig. 5c). The occurrence of humidities in excess of ice saturation was a general feature of the eight study days (Table 3). From an examination of humidity and temperature measurements in Fig. 6c, and from 10 and 11 March (not shown), we

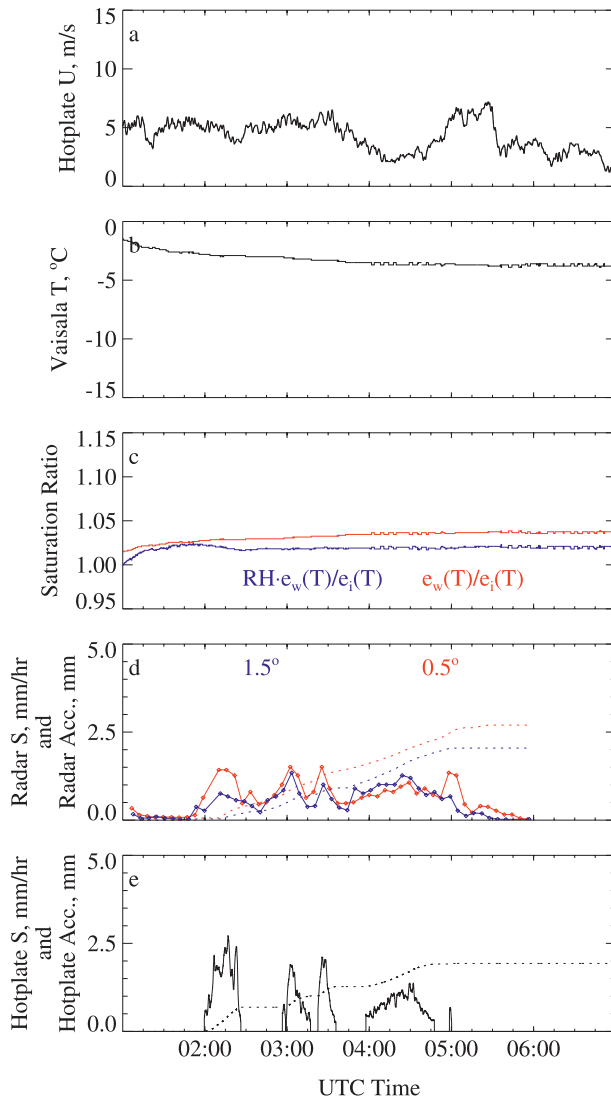


FIG. 5. Time series data from the surface site and the radar on 19 Mar 2006 for (a) Hotplate wind speed, (b) Vaisala temperature, (c) ice saturation ratio and the ratio of the water saturation vapor pressure divided by the ice saturation vapor pressure, (d) radar-derived  $S$  for both tilt angles (from  $Z_e = 110S^2$ , regardless of ray path) and the liquid-equivalent accumulations, and (e) Hotplate  $S$  and the Hotplate liquid-equivalent accumulation.

conclude that approximately 200 m of lift would have produced water saturation on those three days. Those days (16 February and 10 and 11 March) are also the coldest (Table 3). From this we conclude that conditions at low levels on those days were favorable for the appearance of crystals with branched structure and for their development into aggregates (section 3).

Figures 5d and 5e demonstrate that there was good agreement between the Hotplate and radar-derived accumulations on 19 March. In contrast, data from

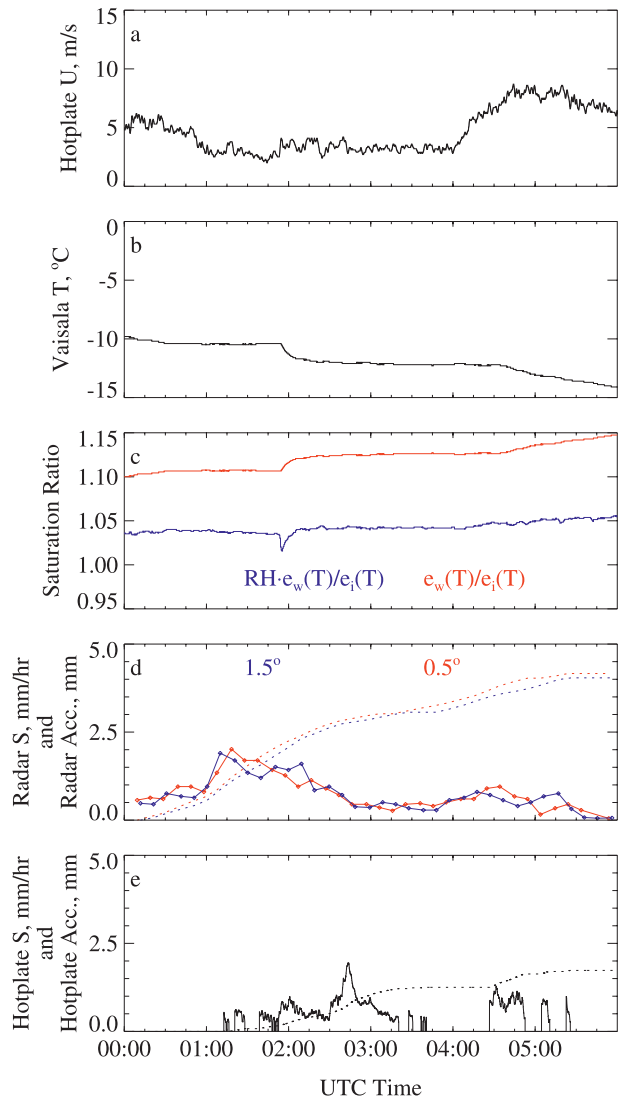


FIG. 6. As in Fig. 5, but for 16 Feb 2006.

16 February reveal that the Hotplate accumulation was substantially less than the radar-derived value (Figs. 6d and 6e). Because the humidities at the surface site were in excess of ice saturation, the accumulation discrepancy on 16 February cannot be attributed to snow-particle sublimation.

An examination of the snow rates in Figs. 6d and 6e helps to explain the accumulation disagreement on 16 February. For an hour interval centered at 0130 UTC, the radar-derived snow rate was substantially larger than its threshold ( $S = 0.30 \text{ mm h}^{-1} \equiv 10 \text{ mm}^6 \text{ m}^{-3}$ ; section 4c) while the Hotplate was reporting  $0.3 < S < 0.7 \text{ mm h}^{-1}$ , or values that were less than its threshold (section 2b). For the same interval (0100 and 0200 UTC), the radar-derived accumulation was approximately 2 mm while the Hotplate accumulation was less than

0.5 mm. There are several explanations for the apparent underestimation by the Hotplate on 16 February. Two conjectures are provided here: 1) processing occurring within the Hotplate electronics negatively biased the reported snow rate—for example, because either the bottom plate power or the catch efficiency correction was positively biased (section 2b; also see Rasmussen et al. 2011), and 2) the Hotplate was unable to respond to the largest particle sizes present within the radar resolution volume (Super and Holroyd 1998). In section 5d we compare radar-derived 24-h accumulations with an independent set of gauges and investigate speculation that the radar-based accumulations are biased.

Before concluding this section, we note that  $Z_e$ - $S$  data from the coldest three days (16 February and 10 and 11 March), when combined into a subset, exhibit a  $Z_e$ - $S$  regression coefficient that is insignificant ( $r = -0.1$ ;  $n = 65$ ;  $p = 0.2$ ). Parts of this subset can be viewed in Figs. 4a and 4c, in Fig. 6d (radar; 16 February), and in Fig. 6e (Hotplate; 16 February). These views of the cold-temperature subset demonstrate that the snow rates were relatively small—nearly all values were less than  $1 \text{ mm h}^{-1}$ —and that the reflectivity variability was substantial ( $10$ – $300 \text{ mm}^6 \text{ m}^{-3}$ ).

### c. Temperature dependence of $\alpha$

From Eq. (3), we hypothesize that  $\alpha$  varies positively with temperature by way of the temperature dependence of  $N$  coming from the inverse temperature dependence of heterogeneous ice nuclei activation. Linkage between temperature and activation is expected from nucleation theory, and two observation-based assessments confirm that behavior. Cooper (1986) analyzed an aircraft dataset, including both wintertime (stratus and cumuli) and summertime (cumuli) observations, and demonstrated that crystal concentrations (on average) vary inversely with temperature. The individual datasets he grouped were acquired in southeastern Wyoming, southwestern Colorado, Montana, Israel, Spain, Australia, and South Africa. Data screening was applied to minimize influence, in the derived  $N$  parameterization, coming from crystals produced by secondary ice production processes. In a separate study, Meyers et al. (1992) fitted ice nuclei measurements conducted in southeastern Wyoming, found them to be consistent with comparable measurements from the United Kingdom, and derived a humidity-dependent ice nucleation parameterization. We interpret the latter as a temperature-dependent function by substituting the parameter in the Meyers et al. scheme—ice supersaturation—with the ice supersaturation evaluated at water saturation. The modes of ice nucleation described by this function are deposition and condensation-freezing. We also use a temperature-dependent

description of contact-freezing nucleation. The latter is based on Meyers et al.'s fit of measurements conducted in southeastern Wyoming. In our implementation of the contact-freezing  $N$  parameterization, we ignore the fact that nucleation can be limited by the rate of attachment of nuclei to cloud droplets (Meyers et al. 1992).

Complicating our attempt to link  $\alpha$  and  $T$ , through the latter's control of  $N$ , is the variability seen in determinations of  $N$  at fixed values of  $T$ . An example of this can be seen in Fig. 2 of Meyers et al. (1992). DeMott et al. (2010) recently established that much of this variability is attributable to spatiotemporal changes of the aerosol and, in particular, to variation of the concentration of aerosol particles that are larger than  $0.5 \mu\text{m}$ . Although we are unable, in our study, to account for aerosol variability, we do note that the Cooper (1986) and the Meyers et al. (1992)  $N$  parameterizations encompass much of the variation in ice nuclei concentration measurements made at  $T > -23^\circ\text{C}$  (DeMott et al. 2010).

Each of the  $N$  parameterizations has temperature as the independent variable, and through Eq. (3) these make  $\alpha$  an increasing function of temperature. This temperature dependence is plotted in Fig. 7 versus a variable that we refer to as surface temperature  $T_S$ . The curves are based on the assumption that the echo-top temperature is the same as the cloud-top temperature  $T_{CT}$  and that the latter is appropriate for predicting the  $N$  in Eq. (3). An additional assumption is that ice crystal concentration, at cloud top, is the same as the snow-particle concentration at the surface. This  $N$ -uniformity constraint excludes situations with a precipitation process that depletes ice crystals (aggregation) and situations associated with a particle-size-dependent fall speed (riming) (section 3). Although the extent of deposition growth relative to the two excluded pathways was not a focus of our investigation (observation of the snow-particle morphology was not attempted), the CoCoRaHS density measurements (section 2c) do argue against a dominating role being played by riming.

The prediction curves seen in Fig. 7 were shifted horizontally to the right from  $T_{CT}$  (cloud-top temperature) to  $T_S$  (surface temperature). For developing this translation, we use the average echo-top height ( $\langle z_{CT} \rangle = 3.4 \text{ km}$ ; Fig. 3), the average potential temperature profile ( $\langle d\theta/dz \rangle$ ; section 4), and the average of the surface-site temperature measurements from  $-10^\circ$  to  $0^\circ\text{C}$  ( $\langle T_{SS} \rangle = -5^\circ\text{C}$ ). The translating equation is  $T_S = T_{CT} + 18$ . In the following paragraph, we explain why surface-site observations with temperature  $< -10^\circ\text{C}$  were eliminated from the averaging. Last, the prediction curves are also based on the same constant value for the ice

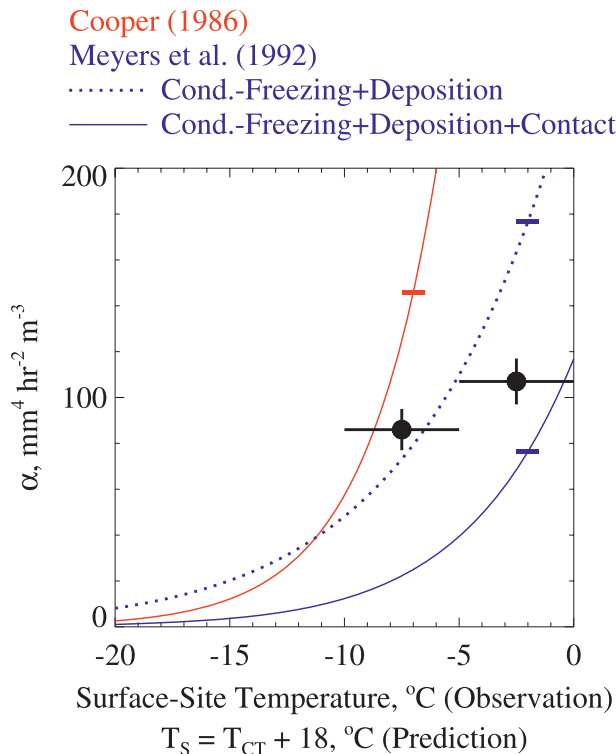


FIG. 7. Predictions of  $\alpha$ , on the basis of Eq. (3), with  $|K_i|^2 = 0.18$ ,  $|K_w|^2 = 0.93$ ,  $\rho_i = 920 \text{ kg m}^{-3}$ ,  $\rho_w = 1000 \text{ kg m}^{-3}$ , and  $V_i = 0.5 \text{ m s}^{-1}$ . The  $N$  parameterization of Cooper (1986), the condensation-freezing + deposition  $N$  parameterization of Meyers et al. (1992), and the condensation-freezing + deposition + contact-freezing  $N$  parameterization of Meyers et al., were used in the predictions. The low-temperature limits of data analyzed by Meyers et al. and Cooper are indicated by rectangles. The black circles indicate  $\alpha$  values that were derived from  $Z_e$ - $S$  observations selected from the surface-site temperature intervals from  $-10^{\circ}$  to  $-5^{\circ}\text{C}$  and from  $-5^{\circ}$  to  $0^{\circ}\text{C}$ . Vertical error bars on the  $\alpha$  observations are the fitting uncertainty [from Eq. (A5)], and the temperature error bars show the surface-site temperature interval.

crystal fall speed. For this we use  $V_i = 0.5 \text{ m s}^{-1}$ , a value representative of the fall speed of branched crystals with  $D > 1 \text{ mm}$  (Mitchell and Heymsfield 2005).

As mentioned in the previous section, three days (16 February and 10 and 11 March) exhibited relatively small values of  $S$  with large  $Z_e$  variability. From Table 3 it is evident that these are the coldest of the eight days, with average temperature (at the surface site) of less than  $-10^{\circ}\text{C}$ . We can tentatively conclude that the surface-site temperature, and the generally small vertical lifting required to reach water saturation (section 5b), are indicative of low-level aggregation during all three of these days. We recall from section 3 that depletion of smaller, more-abundant ice particles is an expectation for aggregation. Because this expectation does not conform

to the  $N$ -uniformity constraint, we have eliminated these three days for the comparison made in Fig. 7.

In Fig. 7 we present two values of  $\alpha$  derived by fitting 124  $Z_e$ - $S$  pairs selected from the surface-site temperature interval from  $-10^{\circ}$  to  $-5^{\circ}\text{C}$  and 141 pairs selected from the surface-site temperature interval from  $-5^{\circ}$  to  $0^{\circ}\text{C}$ . Because we previously demonstrated that retrievals from the two lowest radar tilt angles yield an indistinguishable  $\alpha$  (Figs. 4a and 4c), the reflectivity values in these data subsets come from both the  $0.5^{\circ}$  and  $1.5^{\circ}$  retrievals. The two observational values of  $\alpha$  are seen to plot between prediction limits on the basis of the Cooper (1986) and the Meyers et al. (1992)  $N$  parameterizations. It is also apparent that the observational  $\alpha$  increases with temperature.

We view the comparison of the  $\alpha$  observation, and its prediction, as suggesting a mechanistic link between the  $Z_e$ - $S$  observations and snow-particle genesis. This connection is noteworthy because it implicates a precipitation pathway involving heterogeneous ice nucleation, near cloud top, followed by diffusional growth during sedimentation. Caution is warranted here, for four reasons. First, Eq. (3) demonstrates that the predicted  $\alpha$  is very sensitive to the value picked for  $V_i$ . Our rationale for  $V_i = 0.5 \text{ m s}^{-1}$  is that crystals originating from cloud top, with an estimated temperature of  $-23^{\circ}\text{C}$ , fall through the dendritic growth regime from  $-19^{\circ}$  to  $-11^{\circ}\text{C}$  (section 3) and are resident in that regime for a substantial portion of their fall trajectory. Second, we ignore the fact that in the temperature interval from  $-10^{\circ}$  to  $0^{\circ}\text{C}$  the aggregation efficiency is observed to increase in some circumstances (Mitchell 1988; Field and Heymsfield 2003; also see the review by Pruppacher and Klett 1997). Had this been the case for the snowstorms we investigated, the positive  $\alpha$ - $T$  trend seen in the observations could reflect increased aggregation efficiency for the warmest of the two temperature intervals. Third, the  $\alpha$  predictions in Fig. 7 are based on a temperature-translating equation ( $T_S = T_{CT} + 18$ ) that is derived from an averaged echo-top height, an averaged surface-site temperature, and an averaged potential temperature gradient. The effect of variance in the echo-top height (Fig. 3) can be appreciated by horizontally shifting the prediction curves to be  $6^{\circ}\text{C}$  colder. This shift corresponds to a scenario with an echo-top height that is 1 standard deviation lower than that indicated in Fig. 3. The resulting temperature-translating equation is  $T_S = T_{CT} + 12$ . In that scenario, all three prediction curves are shifted to the left of the observation points and consistency between observation and prediction is less convincing. Fourth, the prediction curves rely on extrapolation of  $N$  to a temperature that is colder than that in the fitted  $N$ - $T$  datasets. The

rectangles placed on the prediction curves, in Fig. 7, indicate the surface-temperature equivalent of the  $N-T$  extrapolation limit. These limits are based on our translation from cloud-top temperature (i.e., the nucleation temperature) to surface temperature by the equation  $T_S = T_{CT} + 18$ . For example, the low-temperature limit in data evaluated by Cooper (1986) is at the sum of  $-7^\circ$  and  $-18^\circ\text{C}$  (i.e.,  $-25^\circ\text{C}$ ).

*d. Radar-derived versus gauge accumulations*

Figure 8 shows 24-h liquid-equivalent accumulations reported by the NWS and the CoCoRaHS; both are plotted versus radar-derived accumulations. The latter come from reflectivity retrievals made over the surface site (along the  $0.5^\circ$  ray path) and require the  $Z_e-S$  relationship (section 5a) and the time-integration method described in section 2d. The NWS accumulations come from an Alter-shielded NWS gauge (Yang et al. 1998) operated at the Cheyenne NWS office, and the CoCoRaHS values are averages of accumulations from the 12 sites described in section 2c. Those averages and their standard deviation are also presented in Table 1. With one exception, all of the CoCoRaHS gauges are located east of the surface site, at a distance of greater than 5 km, and most are located in built-up residential areas with established trees and landscaping. These same surface characteristics are evident in the neighborhoods surrounding the Cheyenne NWS office. In contrast, at the surface site there is a treeless shortgrass prairie and a smaller density of houses (section 2a).

Data scatter seen in Fig. 8 is comparable, in relative terms, to the factor-of-2 variability apparent in the snow-rate comparisons (Figs. 4b and 4d). Because a 24-h integration of snow rate is expected to reduce scatter that is due to the imperfect radar and surface-site time synchronization, the variance evident in Fig. 8 must be explained. We surmise that an important contributor is variation inherent to the precipitation field within the Cheyenne region. We interpret the relative error associated with the CoCoRaHS averages, approximately  $\pm 0.45$ , as reflecting this variability and note that its magnitude is sufficient to make the CoCoRaHS points overlap, or nearly overlap, the one-to-one line.

It is also evident that a majority of the NWS accumulations are greater than the CoCoRaHS averages. This could be a consequence of the larger snow-particle catch efficiency of the Alter-shielded NWS gauge relative to the unshielded CoCoRaHS gauge, but results from 15 February are inconsistent with this conjecture. Last, the departure of the  $y = ax$  fit line from unity indicates that (on average) the NWS and CoCoRaHS gauges reported more accumulation than the radar-derived

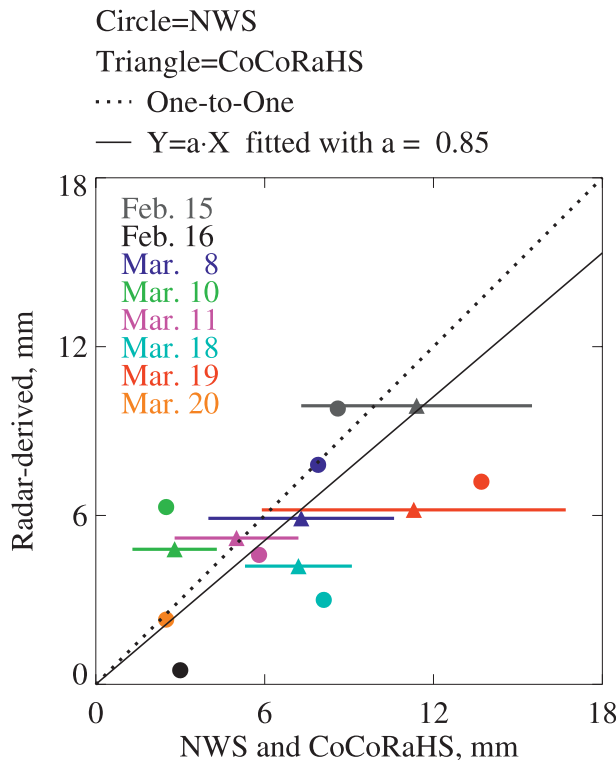


FIG. 8. Comparison of gauge and radar-derived liquid-equivalent 24-h accumulations. Radar reflectivities are from over the surface site along the  $0.5^\circ$  ray path. The  $Z_e-S$  relationship used to derive the snow rate is  $Z_e = 110S^2$  (section 5a). The NWS accumulations (circles) come from the Alter-shielded gauge operated at the Cheyenne NWS office. The CoCoRaHS accumulations (triangles) are plotted with error limits that extend from the average minus 1 standard deviation to the average plus 1 standard deviation. The CoCoRaHS gauges are unshielded.

values. Because the latter were calibrated with the Hotplate, this 15% bias may be a consequence of the factors discussed in section 5b, or it could reflect the different surface characteristics at the surface site when compared with those at the NWS and CoCoRaHS sampling locations.

**6. Summary and conclusions**

This work is significant because it supplements the small number of empirical  $Z_e-S$  relationships that are available for the high-altitude NWS radars. Previous determinations are available for NWS radars at Denver ( $\alpha = 147$ ;  $\beta = 2$ ), and Grand Mesa, Colorado ( $\alpha = 35$ ;  $\beta = 2$ ) (Super and Holroyd 1998). These radar sites are at 1676- and 3059-m altitude, respectively, and thus are comparable to Cheyenne (altitude 1886 m). In addition, Super and Holroyd also report values of  $\alpha$  for three low-altitude radars. For that subset, the values at Minneapolis, Minnesota ( $\alpha = 173$ ;  $\beta = 2$ ), and Cleveland,

Ohio ( $\alpha = 304$ ;  $\beta = 2$ ), exceed Albany, New York ( $\alpha = 125$ ;  $\beta = 2$ ). All five of the determinations reported by Super and Holroyd are for a range of 20–40 km and for a gate height that is relatively small for Denver (370 m), Minneapolis (340 m), and Cleveland (340 m) and is larger for Grand Mesa (960 m) and Albany (880 m). Because Super and Holroyd (their Fig. 5) also demonstrated that values of  $\alpha$  decrease with range—because of the climatological tendency for  $dZ_e/dz$  to be negative—it follows that the  $\alpha$  they report for Grand Mesa and Albany would be about a factor of 2 larger if extrapolated to the lower gate heights interrogated at the other three sites. This would nudge Grand Mesa's  $\alpha$  closer to that of Denver and Albany's  $\alpha$  closer to those of the two other low-altitude sites. Our result for Cheyenne ( $\alpha = 110$ ;  $\beta = 2$ ) is then reasonably consistent with the two high-altitude values reported by Super and Holroyd, and with an apparent separation between high-altitude and low-altitude  $\alpha$ s. Because the semiempirical theory developed by Matrosov (1992) indicates that  $\alpha$  can increase with decreasing air/ice-particle density, it is conceivable that the low-altitude sites are more affected by snowfall produced by aggregation or that the high-altitude sites are more affected by riming. This interpretation deserves further examination because Matrosov also states that the  $\alpha$ –density relationship can be reversed with realistic perturbations of the  $V_r$ – $D$  relationship.

As we discussed in section 1, low-level radar retrieval of the reflectivity can be limited by terrain. Although WSR blockage is apparent in our ray-path plot (Fig. 1), the suspected bias does not stand out in our comparison of the low-level reflectivity vertical gradients assessed close to the WSR and over the surface site. Related to this, we see no substantial difference in the two values of  $\alpha$  that we derive over the surface site at the  $0.5^\circ$  and  $1.5^\circ$  tilt angles.

Our other result comes from an analysis of a subset of  $Z_e$ – $S$  pairs associated with warm temperatures (surface-site temperature  $> -10^\circ\text{C}$ ). The two derived values of  $\alpha$  exhibit a positive temperature dependence (Fig. 7) and are bracketed by prediction curves based on Eq. (3). This consistency, between prediction and observation, is the basis for our assertion that  $\alpha$  varies inversely with ice-particle number concentration and that this dependence could be the result of ice nucleation occurring at the top of the investigated snowstorms. A practical outcome is that Eq. (3), combined with measurement of snow-particle concentration and selection of cases with particle morphology that is amenable to Eq. (3) (particles with a fall speed that is approximately independent of  $D$ ), may constitute an avenue for determining  $\alpha$  in situations that are dominated by precipitation produced

by either vapor deposition or aggregation. This method of determining  $\alpha$  would not rely on measurement of precipitation intensity and would thus be an alternative to the approach taken here.

*Acknowledgments.* We are indebted to Sam Haimov and Bart Geerts for the benefit of several discussions and especially for their assistance with our analysis of the WSR dataset. The advice of David Leon and two anonymous reviewers helped to sharpen the presentation; we appreciate their persistence. Our field measurements would not have been possible without the expert technical assistance provided by Matt Burkhart. Support from Grants WWDC49564 (Wyoming Water Development Commission) and DOIUSGS43613PRE (U.S. Department of Interior) is gratefully acknowledged. Also, J. Snider's involvement in the analysis phase of the project was supported by the National Science Foundation through Grant ATM-0650609.

## APPENDIX

### Statistical Methods Used to Deduce the $Z_e$ – $S$ Relationship

Described here are the statistical tools we used to derive three estimates of the leading coefficient in Eq. (1). Each approach starts with the paired sets  $Z_e$  and  $S^2$ . The first takes  $Z_e$  to be the dependent variable and employs a least squares procedure called “curvefit” (Interactive Data Language; ITT Visual Information Solutions) that iteratively minimizes the sum of the squares of the departure of the data points from the best-fit line. The calculation proceeds through three steps: 1) A provisional value of  $\alpha_1$  is produced when curvefit is initialized with equal weighting applied to all data points, and the resulting  $\alpha_1$  is used to evaluate weights as either the reciprocal of the absolute value of the departure or  $0.10 \text{ m}^3 \text{ mm}^{-6}$ . The larger of the two values is chosen as the weight. 2) Curvefit is applied again, with weights set equal to the value chosen in step 1, and the new estimate of  $\alpha_1$  is used to update the weights as in step 1. 3) Step 2 is repeated until the absolute value of the relative change of  $\alpha_1$  is less than 0.01. It can be shown that these steps converge to a solution that minimizes the sum of the absolute value of the departures, as opposed to the least squares approach of minimizing the sum of the squares of the departures. Our approach is preferred because it deemphasizes the influence of outlying data points (Aster et al. 2005).

The value of  $\alpha_2$  is derived as described for  $\alpha_1$ ;  $S^2$  is taken to be the dependent variable, however, and the resulting fit coefficient  $\gamma_2$  is converted to an “alpha”

(i.e.,  $\alpha_2 = 1/\gamma_2$ ). The lower limit for the weight (i.e., in steps 1 and 2) is taken to be  $3.3 \text{ h mm}^{-1}$ .

The values of  $\alpha_1$  and  $\gamma_2$  are used to derive the standard errors as

$$\sigma_{\alpha_1} = \sqrt{\frac{\sum(Z_e - \alpha_1 S^2)^2}{N \left[ \sum S^4 - \frac{1}{N} (\sum S^2)^2 \right]}}, \quad (\text{A1})$$

$$\sigma_{\gamma_2} = \sqrt{\frac{\sum(S^2 - \gamma_2 Z_e)^2}{N \left[ \sum Z_e^2 - \frac{1}{N} (\sum Z_e)^2 \right]}}, \quad \text{and} \quad (\text{A2})$$

$$\sigma_{\alpha_2} = \frac{1}{\gamma_2^2} \sigma_{\gamma_2}. \quad (\text{A3})$$

Here,  $N$  is now the total number of data points and Eq. (A3) employs propagation of error (Young 1962) to derive the  $\alpha_2$  standard deviation from the values of  $\gamma_2$  and  $\sigma_{\gamma_2}$ .

The third approach is based on the principle of maximum likelihood applied to logarithmically transformed sets of  $Z_e$  and  $S^2$ . From consideration of the principle of maximum likelihood (Young 1962), it can be shown that the fit coefficient is

$$\alpha_3 = \exp(\langle \ln Z_e \rangle - \langle \ln S^2 \rangle). \quad (\text{A4})$$

Here,  $\langle \ln Z_e \rangle$  and  $\langle \ln S^2 \rangle$  are averages of the logarithmically transformed sets of  $Z_e$  and  $S^2$ , and the standard error is

$$\sigma_{\alpha_3} = \sqrt{\frac{\alpha_3^2 \sum (\ln Z_e - \ln \alpha_3 - \ln S^2)^2}{N^2}}. \quad (\text{A5})$$

REFERENCES

Aster, R., B. Borchers, and C. Thurber, 2005: *Parameter Estimation and Inverse Problems*. Academic Press, 320 pp.

Battan, L. J., 1973: *Radar Observations of the Atmosphere*. University of Chicago Press, 324 pp.

Boatman, J. F., and R. F. Reinking, 1984: Synoptic and mesoscale circulations and precipitation mechanisms in shallow upslope storms over the western high plains. *Mon. Wea. Rev.*, **112**, 1725–1744.

Boucher, R. J., and J. G. Wieler, 1985: Radar determination of snowfall rate and accumulation. *J. Climate Appl. Meteor.*, **24**, 68–73.

Braham, R. R., 1990: Snow particle size spectra in lake effect snows. *J. Appl. Meteor.*, **29**, 200–207.

Brown, P. R. A., and P. N. Francis, 1995: Improved measurements of ice water content in cirrus using a total-water probe. *J. Atmos. Oceanic Technol.*, **12**, 410–414.

Brown, R. A., V. T. Wood, and T. W. Barker, 2002: Improved detection using negative elevation angles for mountaintop

WSR-88Ds: Simulation of KMSX near Missoula, Montana. *Wea. Forecasting*, **17**, 223–237.

Chrisman, J. N., and C. A. Ray, 2006: A first look at the operational (data quality) improvements provided by the open radar data acquisition (ORDA) system. Preprints, *32nd Conf. on Radar Meteorology*, Albuquerque, NM, Amer. Meteor. Soc., P4R.10. [Available online at <http://ams.confex.com/ams/pdfpapers/96225.pdf>.]

Cooper, W. A., 1986: Ice initiation in natural clouds. *Precipitation Enhancement—A Scientific Challenge, Meteor. Monogr.*, No. 43, Amer. Meteor. Soc., 29–32.

Crum, T. D., R. L. Alberty, and D. W. Burgess, 1993: Recording, archiving, and using WSR-88D data. *Bull. Amer. Meteor. Soc.*, **74**, 645–653.

DeMott, P. J., and Coauthors, 2010: Predicting global atmospheric ice nuclei distributions and their impact on climate. *Proc. Natl. Acad. Sci. USA*, **107**, 11 217–11 222.

Field, P. R., and A. J. Heymsfield, 2003: Aggregation and scaling of ice crystal size distributions. *J. Atmos. Sci.*, **60**, 544–560.

Fujiyoshi, Y., and G. Wakahama, 1985: On snow particles comprising an aggregate. *J. Atmos. Sci.*, **42**, 1667–1674.

—, T. Endoh, T. Yamada, K. Tsuboki, Y. Tachibana, and G. Wakahama, 1990: Determination of a Z–R relationship for snowfall using a radar and high sensitivity snow gauges. *J. Appl. Meteor.*, **29**, 147–152.

Gordon, G. L., and J. D. Marwitz, 1986: Hydrometeor evolution in rainbands over the California valley. *J. Atmos. Sci.*, **43**, 1087–1100.

Groisman, P. Y., and D. R. Legates, 1994: The accuracy of United States precipitation data. *Bull. Amer. Meteor. Soc.*, **75**, 215–227.

Gunn, K. L. S., and J. S. Marshall, 1958: The distribution with size of aggregate snowflakes. *J. Meteor.*, **15**, 452–461.

Ice, R. L., and Coauthors, 2007: Optimizing clutter filtering in the WSR-88D. Preprints, *23rd Int. Conf. on Interactive Information Processing Systems for Meteorology, Oceanography and Hydrology*, San Antonio, TX, Amer. Meteor. Soc., P2.11. [Available online at <http://ams.confex.com/ams/pdfpapers/116863.pdf>.]

Joss, J., and A. Waldvogel, 1990: Precipitation measurement and hydrology. *Radar in Meteorology*, D. Atlas, Ed., Amer. Meteor. Soc., 577–606.

Judson, A., and N. Doesken, 2000: Density of freshly fallen snow in the central Rocky Mountains. *Bull. Amer. Meteor. Soc.*, **81**, 1577–1587.

King, W. D., D. A. Parkin, and R. J. Handsworth, 1980: A hot-wire liquid water device having fully calculable response characteristics. *J. Appl. Meteor.*, **17**, 1809–1813.

Knight, C. A., and L. Miller, 1993: First radar echoes from cumulus clouds. *Bull. Amer. Meteor. Soc.*, **74**, 179–188.

Kollias, P., E. E. Clothiaux, M. A. Miller, B. A. Albrecht, G. L. Stephens, and T. P. Ackerman, 2007: Millimeter-wavelength radars: New frontier in atmospheric cloud and precipitation research. *Bull. Amer. Meteor. Soc.*, **88**, 1608–1624.

Lo, K. K., and R. E. Passarelli Jr., 1982: The growth of snow in winter storms: An airborne observational study. *J. Atmos. Sci.*, **39**, 697–706.

Matrosov, S. Y., 1992: Radar reflectivity in snowfall. *IEEE Trans. Geosci. Remote Sens.*, **30**, 454–461.

—, M. D. Shupe, and I. V. Djalalova, 2008: Snowfall retrievals using millimeter-wavelength cloud radars. *J. Appl. Meteor. Climatol.*, **47**, 769–777.

Melnikov, V., P. B. Chilson, and D. B. Mechem, 2009: Extending the capabilities of the polarimetric WSR-88D: Observations of

- cirrus clouds and moist layers. Preprints, *34th Conf. on Radar Meteorology*, Williamsburg, VA, Amer. Meteor. Soc., P3.1. [Available online at <http://ams.confex.com/ams/pdfpapers/155817.pdf>.]
- Meyers, M. P., P. J. DeMott, and W. R. Cotton, 1992: New primary ice-nucleation parameterizations in an explicit cloud model. *J. Appl. Meteor.*, **31**, 708–721.
- Miller, M. A., J. Verlinde, C. V. Gilbert, G. J. Lehenbauer, J. S. Tongue, and E. E. Clothiaux, 1998: Detection of non-precipitating clouds with the WSR-88D: A theoretical and experimental survey of capabilities and limitations. *Wea. Forecasting*, **13**, 1046–1062.
- Mitchell, D. L., 1988: Evolution of snow-size spectra in cyclonic storms. Part I: Snow growth by vapor deposition and aggregation. *J. Atmos. Sci.*, **45**, 3431–3451.
- , and A. J. Heymsfield, 2005: Refinements in the treatment of ice particle terminal velocities, highlighting aggregates. *J. Atmos. Sci.*, **62**, 1637–1644.
- Moismann, L., 1995: An improved method for determining the degree of snow crystal riming by vertical Doppler radar. *Atmos. Res.*, **37**, 305–323.
- Ohtake, T., 1970: Factors affecting the size distribution of raindrops and snowflakes. *J. Atmos. Sci.*, **27**, 804–813.
- Pokharel, B., and G. Vali, 2011: Evaluation of collocated measurements of radar reflectivity and particle sizes in ice clouds. *J. Appl. Meteor. Climatol.*, **50**, 2104–2119.
- Pruppacher, H. R., and J. D. Klett, 1997: *Microphysics of Clouds and Precipitation*. 2nd ed. Kluwer, 976 pp.
- Rasmussen, R., M. Dixon, S. Vasiloff, F. Hage, S. Knight, J. Vivekanandan, and M. Xu, 2003: Snow nowcasting using a real-time correlation of radar reflectivity with snow gauge accumulation. *J. Appl. Meteor.*, **42**, 20–36.
- , J. Hallett, R. Purcell, S. D. Landolt, and J. Cole, 2011: The Hotplate precipitation gauge. *J. Atmos. Oceanic Technol.*, **28**, 148–164.
- Rogers, R. R., and M. K. Yau, 1989: *A Short Course in Cloud Physics*. 3rd ed. Pergamon Press, 304 pp.
- Schmidt, R. A., 1982: Vertical profiles of wind-speed, snow concentration, and humidity in blowing snow. *Bound.-Layer Meteor.*, **23**, 223–246.
- Sevruk, B., 1996: Adjustment of tipping-bucket precipitation gauge measurements. *Atmos. Res.*, **42**, 237–246.
- Smith, P. L., 1984: Equivalent radar reflectivity factors for snow and ice particles. *J. Climate Appl. Meteor.*, **23**, 1258–1260.
- , 1998: On the minimum useful elevation angle for weather surveillance radar scans. *J. Atmos. Oceanic Technol.*, **15**, 841–843.
- Super, A. B., and E. W. Holroyd, 1998: Snow accumulation algorithm for the WSR-88D radar, final report. Bureau of Reclamation Rep. R-98-05, 75 pp.
- Vignal, B., G. Galli, J. Joss, and U. Germann, 2000: Three methods to determine profiles of reflectivity from volumetric radar data to correct precipitation estimates. *J. Appl. Meteor.*, **39**, 1715–1726.
- Wang, P. K., and W. Ji, 2000: Collision efficiencies of ice crystals at low-intermediate Reynolds numbers colliding with supercooled cloud droplets: A numerical study. *J. Atmos. Sci.*, **57**, 1001–1009.
- Wetzel, M., and Coauthors, 2004: Mesoscale snowfall prediction and verification in mountainous terrain. *Wea. Forecasting*, **19**, 806–828.
- Wolfe, J. P., 2007: Radar-estimated upslope snowfall rates in southeastern Wyoming. M.S. thesis, Dept. of Atmospheric Science, University of Wyoming, 64 pp.
- Wood, V. T., R. A. Brown, and S. V. Vasiloff, 2003: Improved detection using negative elevation angles for mountaintop WSR-88Ds. Part II: Simulations of the three radars covering Utah. *Wea. Forecasting*, **18**, 393–403.
- Yang, D., B. E. Goodison, J. R. Metcalfe, V. Golubev, R. Bates, T. Pangburn, and C. L. Hanson, 1998: Accuracy of NWS 8" standard nonrecording precipitation gauge: Results and application of WMO Intercomparison. *J. Atmos. Oceanic Technol.*, **15**, 54–68.
- Young, H. D., 1962: *Statistical Treatment of Experimental Data*. McGraw-Hill, 172 pp.